Design and Validation of a Multimode Multifrequency VHF/UHF Airborne Radar

C. Papa, G. Alberti, G. Salzillo, G. Palmese, D. Califano, L. Ciofaniello, M. Daniele,
C. Facchinetti, F. Longo, R. Formaro,
I. Catapano, L. Crocco, G. Gennarelli, and F. Soldovieri

***Abstract*- This letter deals with the design, realization and validation of a multimode/multifrequency airborne radar designed for both surface and subsurface prospections. The system operates in the frequency band from VHF to UHF and works in two different modes: i) nadir-looking sounder in the VHF band (163 MHz carrier frequency); ii) side-looking imager (SAR) in the UHF band with two channels at 450 MHz and 860 MHz, respectively. The system validation has been carried out for the "sounder" mode thanks to helicopter borne surveys carried out over an area of Campania region, Southern Italy. The surveys have provided a first proof of system capability in obtaining useful information about the surface and shallower subsurface layers over a large scale and in a relatively short time. In particular, the data collected by the sounder have been processed by means of a microwave tomographic reconstruction approach and features consistent with tunnels buried at a depth of 15 m have been identified.**

***Index Terms*—VHF/UHF airborne radar, microwave tomographic approach, surface imaging, subsurface prospections.**

I. INTRODUCTION

In recent years, large attention has been devoted to the development and use of airborne radars working in the frequency range from VHF to UHF band (e.g. see [1]-[7]). The combination of low frequencies and good relative bandwidth makes these systems of interest in civilian and security applications. The main application areas regard forestry applications, biomass measuring and monitoring, archaeological and geological exploration, glaciers investigation, detection and localization of buried targets. In addition, these kinds of systems are suitable even for non-civil applications as sub-surface target detection and foliage penetration. The development of these systems entails technological and scientific efforts for design stage regarding antennas, low noise amplifiers, band-pass filters, digital receiver technology as well as data-processing algorithms. In this framework, the Italian Space Agency (ASI) has promoted and funded the development of a new multimode/ multifrequency airborne radar able to operate as a nadir-looking sounder in the VHF band and a side-looking imager in the UHF band. This system can be seen not only as a "proof of concept" for next Earth observation and planetary exploration space missions, but even as a validation tool for civil and non-civil VHF/UHF radar terrestrial diagnostics, imaging and monitoring applications. The research consortium CO.RI.S.T.A. had in charge the design, realization and in-flight validation of the system. In this letter, we present the above mentioned radar system and the operative validation of its capabilities for the sounder modality. To support this goal, a model-based microwave tomographic approach, recently developed by IREA-CNR [8, 9], has been used to process the measurements acquired during flight surveys with the aim to enhance the interpretability of the raw-data radar images.

The letter is organized as follows. Section II describes the main features of the radar system. Section III recalls the microwave imaging approach. The measurement results and the corresponding tomographic reconstructions are reported in Sec. IV. Finally, concluding remarks are provided in Sec. V.

II. DESCRIPTION OF THE RADAR SYSTEM

The radar system exploits three different frequency bands for both subsurface and SAR imaging capabilities. In the sounder mode, the radar operates with a 163 MHz carrier frequency and a bandwidth of 10 MHz. In SAR mode, two frequency ranges are used for lower and higher resolution imagers. The lower resolution SAR (SAR-Low) imager works at 450 MHz with a 40 MHz bandwidth, whereas the higher resolution SAR (SAR-High) imager operates at 860 MHz with a bandwidth of 80 MHz. In both sounder and imager modes, a linear frequency modulated (LFM, also called chirp) signal is transmitted, where the bandwidth is synthesized in the imager mode by a stepped chirp with a bandwidth step of 10 MHz [10], where the center frequency of each sub-band is stepped pulse-by-pulse.

The system is composed by three main blocks (see Fig. 1): the Radar Digital Unit (RDU), the Radio Frequency Unit (RFU), and the Power Supply Unit (PSU). RDU has in charge the parameters setting, timing generation and data handling. It is a full programmable digital unit including the Analog to Digital

C. Papa, G. Alberti, G. Salzillo, G. Palmese, D. Califano, L. Ciofaniello, and M. Daniele are with the Consorzio di Ricerca su Sistemi di Telesensori Avanzati (CO.RI.S.T.A.), Naples, Italy.

C. Facchinetti, F. Longo, and R. Formaro are with the Italian Space Agency (ASI), Rome, Italy.

I. Catapano, L. Crocco, G. Gennarelli, and F. Soldovieri are with the Institute for Electromagnetic Sensing of the environment, Italian Research Council, Naples, Italy. (e-mail: soldovieri.f@irea.cnr.it)

Converter (ADC) and data storage unit. RFU embeds the Frequency Generation Unit (FGU), which has the task to generate all synchronisms and RF signals, and the Digital Signal Processor (DSP) that generates the Low Frequency Modulated (LFM) signal chirp. The PSU provides the power supply to whole system by an external 28 V DC voltage.

The architecture of the system is depicted in Fig. 2. The design was conceived so that most building blocks are shared by both sounder and imager functionalities. Base band signal generation, base band data sampling and data handling are common to both sounder and imager operational modes. This represents the main feature of the entire system and a great advantage is gained by the use of the same ADC, thanks to the usage of an under-sampling technique. The system settings for the different functional modalities are described as follows:

Sounder mode: 10 MHz transmitted bandwidth centered on a 163 MHz carrier. The transmitted signal is generated by the FGU as LFM signal with the starting frequency at 158 MHz.

SAR-Low: stepped 40 MHz transmitted bandwidth is synthetized by four sub-bands of 10 MHz transmitted over four carriers. The carriers differ of 10 MHz each other, so that no overlap arises between the transmitted sub-bands. By considering the four frequency sub-bands, the transmitted signal covers the frequency range [430, 470] MHz.

SAR-High: a stepped 80 MHz transmitted bandwidth is synthesized by eight sub-bands of 10 MHz transmitted over eight carriers with an overall frequency range [820, 900] MHz.

As shown in Fig. 2, the Tx and Rx blocks are common to both the sounder and imager operative modes, with the only difference in the frequency up-conversion. The Tx block performs base band signal generation and the base band signal is the Sounder signal itself. The chains UHF–Low, UHF-High, VHF, depicted in Fig. 2, work in an exclusive way.

The VHF band corresponds to Sounder operative mode and performs base band signal amplification only.

The UHF-High and UHF-Low blocks perform base band signal up-conversion to working frequencies, when corresponding operational mode are selected. The Rx block performs anti-aliasing data filtering and data sampling after frequency down-conversion, which is necessary only for Imager mode. The designed architecture permits a high flexibility of the system in terms of transmitted bandwidth, so that the radar can be easily upgraded to transmit a wider bandwidth.

As regards the Rx chain, after the down-conversion in the SAR-Low and SAR-High receiving chains, the IF signal is centered at 163 MHz covering [158-168] MHz bandwidth. Then, the incoming signal is sampled by the ADC at 100 MHz using the under-sampling technique. Therefore, the sampled spectrum is a replica at IF of the main one. This solution ensures the advantage to use the same ADC for the three different frequency carriers (163, 450 and 860 MHz).

An auto check functional mode has been implemented so to carry out an internal calibration. Specifically, a high speed and high attenuation switch reroutes the transmitted signal on the Rx chain bypassing the antenna. The auto check mode may be switched on, manually, every time during the mission, with

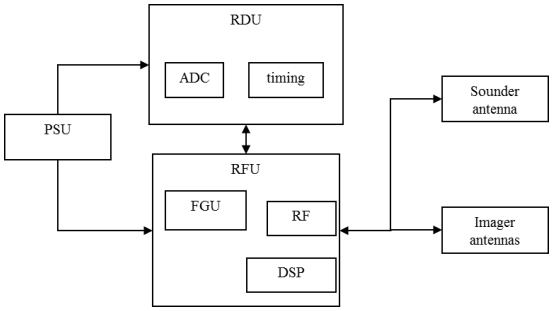

Figure 1. Block diagram of the radar system.

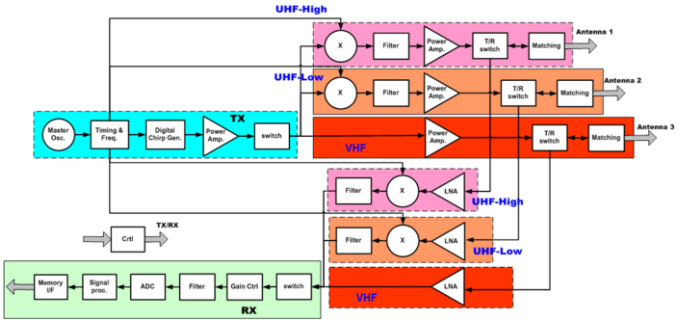

Figure 2. General architecture of the system.

the exception of the acquisition stage. Platform altitude and geo-referencing are ensured by external GPS/INS linked by serial port to the RDU.

The nominal parameters of the three radars are listed in Tab. I. Table II summarizes the nominal radar performances with the indication also of the azimuth ambiguity ratio (AASR) and the range ambiguity ratio (RASR).

Three antenna systems have been adopted for the different functionalities. The sounder antenna is a log periodic one with four radiating elements. The imager antennas are planar patch array designed and realized by University of Calabria, Italy. Figure 3 shows the sounder and imager antennas installed on the civil helicopter (Eurocopter AS350), used for the surveys here presented.

Both data from the sounder and imager are pre-processed by an *ad-hoc* configurable software. Focusing is the core of the data processing, which is based on the well assessed Chirp Scaling Algorithm (CSA) [11-14]. Due to Doppler bandwidth oversampling, a data pre-summing is performed in order to increase signal to noise ratio. Other pre-processing features are related to interferences identification and suppression [15]. Furthermore, the Phase Gradient Autofocus (PGA) algorithm allows for the motion compensation [16-20], which is relevant to imager data processing. Doppler parameter estimation is necessary for data processing and is achieved by data itself jointly with auxiliary information from the GPS/INS navigation system.

In this work, we use a model-based imaging scheme based on a microwave tomographic approach to achieve focused images for the sounder mode. Therefore, only the basic range compression and Hanning sidelobe suppression function has been performed in the pre-processing of the sounder data.

TABLE I
SYSTEM PARAMETERS

	Sounder	SAR-Low	SAR-High
Altitude	>1300 m	>1000 m	>1000 m
Carrier	163 MHz	450 MHz	860 MHz
Tx bandwidth	10 MHz	40 MHz	80 MHz
Tx steps	1x10 MHz	4x10 MHz	8x10 MHz
PRF	500 Hz	2000 Hz	4000 Hz
Pulse width (single step)	3.3 μs		
Rx window width	10 μs	8.03 μs	8.03 μs
Antenna type	Periodic Log	Planar array of 4 x 1 patch	Planar array of 8 x 2 patch, dual polarization
Antenna gain	7 dB	17 dB	19 dB
Elevation pointing	Nadir	45°	
Azimuth pointing	Nadir	0°	
Range aperture	68°	75°	37°
Azimuth aperture		20°	10°
ADC Sampling frequency	50 MHz/100MHz		
Peak power	200W		

TABLE II
NOMINAL PERFORMANCES

	Sounder	**SAR Low**	**SAR High**
Across track resolution	10-100 m		
Range resolution (free space)	15 m	3.75 m (stepped)	1.87 m (stepped)
Along track resolution	7-75 m @ 800m 27-280 m @ 3000m.	4.8 m @ 4 looks	2.5 m @ 2 looks
Penetration Depth	100 m (moderate attenuation)	Foliage penetration	
Maximum Swath (geometrical)	2000 m @ 800m 7000 m @ 3000m	7400m@1000m	1500m@1000m
AASR		No appreciable at chosen PRF	No appreciable at chosen PRF
RASR		-55 dB	-62 dB

Figure 3. The sounder and imager antennas mounted on the civil helicopter.

III. MICROWAVE TOMOGRAPHIC APPROACH

An imaging method has been recently proposed in [8, 9] with the aim of enhancing the interpretability of the radargrams collected by an airborne platform. This tomographic method belongs to the class of the linearized inverse scattering approaches; it is based on the Born approximation and exploits a simple ray based model to cast the relationship between the backscattered field and the unknown electric contrast, i.e. the function that expresses the difference between the targets' permittivity and the permittivity of the background scenario.

Here, the inversion scheme is further simplified by assuming that propagation occurs in free-space, i.e. neglecting the effect of the air-soil interface. This choice is due to two considerations. First of all, propagation in the ground is much less significant than the one in free-space (especially if detection of shallow target is concerned), so that distortion effects due to an inaccurate modeling of the underground wave propagation path are negligible. Secondly, the radar, even when operated in the sounder mode, can be used to localize surface objects, hence such a simplification of the algorithm allows its immediate use also for this purpose.

The inversion method assumes a 2D geometry in which the objects are invariant along the *y*-direction and are hosted in the investigation domain $\Omega \in [-a,a]\times[z_1,z_2]$. Thus, in the adopted reference system, the *x*-axis is parallel to the flight trajectory and the *z*-axis is the nadir direction [9]. The transmitting and receiving antennas are co-located and move along a linear trajectory Γ, whose distance from the investigation domain Ω is fixed by accounting for the average flying height of the airborne platform. For each position $(x_s, z_s) \in \Gamma$, the transmitting antenna radiates a transverse magnetic (TM) polarized incident electric field in the frequency interval $f \in [f_{\min}, f_{\max}]$. For such multi-monostatic/multi-frequency measurement configuration, the relation to be inverted reads as

$$E_S(x_S, z_S, f) = \int_{-a}^{a}\int_{z_1}^{z_2} \frac{\exp(-j2\beta_0 R)}{R}\chi(x',z')\,dx'dz' \qquad (1)$$

wherein $E_S(x_S, z_S, f)$ is the field backscattered in (x_S, z_S) at the frequency f, $R=\sqrt{(x_s-x')^2+(z_s-z')^2}$ is the distance from the antenna to the point (x', z') in Ω, β_0 is the wave-number in free-space and

$$\chi(x',z') = \varepsilon_T(x',z')/\varepsilon_0 - 1 \qquad (2)$$

is the contrast function, being $\varepsilon_T(x',z')$ the equivalent permittivity of the target. After discretization, the problem turns into the inversion of the matrix equation:

$$\underline{\mathbf{E_S}} = \underline{\underline{\mathbf{L}}}\,\underline{\chi} \qquad (3)$$

where $\underline{\mathbf{E_S}}$ is the $M = P\times F$ complex data vector (P is the number of Tx/Rx positions and F is the number of frequencies); $\underline{\chi}$ is a N-dimensional vector of complex elements where N is the number of pixels in Ω, and $\underline{\underline{\mathbf{L}}}$ is a $M\times N$ matrix. The Truncated Singular Value Decomposition (TSVD) is adopted as a regularization scheme to ensure a stable solution, i.e., avoid that the tomographic image is affected by the amplification of errors on data [21]. In order to apply the above described method to the radar sounder, a preprocessing has been performed to make the collected range compressed measurements suitable for the inversion in frequency domain [8].

IV. EXPERIMENTAL RESULTS AND DISCUSSION

The sounder functionality has been tested in operative conditions thanks to a flight campaign in the southern part of

Campania region, Southern Italy. Here, we report the tomographic reconstructions relevant to a hilly area covering a segment of a highway. The hilly terrain is a clay soil, which was dry at the time of the surveys. The site has been selected to have preliminary indications on the sounder capability to reconstruct the terrain topography and possibly to detect subsurface targets in challenging operative conditions.

Before analyzing the results, note that the relatively low gain of the deployed antenna arises also echoes from the surface at directions different from nadir (see the maximum swath in Tab. II). In addition, the 15 m range-resolution entails that the main reflection accounts not only for the surface contribution in nadir direction but even for the lateral surface contribution till to a distance of about 200 m. This value is estimated by considering a nominal height of the airborne platform at about 1300 m, which was a good approximation of the flight quota during the survey.

The first track is shown in the first panel of Fig. 6; it is delimited by points A and B and is about 1200 m long. The elevation profile provided by Google Earth is reported in the second panel of Fig. 6. To apply the tomographic data processing, the radargram has been partitioned into subsets and the 10 MHz bandwidth has been discretized with a step of 0.5 MHz. The threshold of the TSVD has been selected to filter out the singular values whose magnitude is lower than -10 dB with respect to the maximum one. The tomographic reconstructions in the third and fourth panels of Fig. 6 are plotted versus measurement abscissa and by assuming a free-space electromagnetic velocity. The image in third panel has been saturated to better appreciate the capability of the system to characterize the terrain topography. As can be seen, the shape of the hill overhanging the highway is in good agreement with the elevation profile provided by Google Earth. The reconstruction in the fourth panel shows that a significant reflection appears between the beginning and 400 m of the profile. This is due to the lateral reflections caused by man-made constructions as the dump at the beginning of the profile and the area of the tunnel entrance. Between 400 and 800 m, the area is not covered by structures so that the radar signal accounts mainly for the soil and vegetation reflection. Finally, in the last part of the profile, we observe again strong reflections due to the presence of a road. Moreover, between about 900 and 1000 m, a lateral contribution arises for the presence of the hillock (change of the slope occurring at about 1000 m) beyond the road.

The second scan between the points C and D is shown in the first panel of Fig. 7. The figures in the second and third panel confirm that the radar is still able to provide a good reconstruction of the terrain topography. The reconstruction reported in fourth panel shows that the reflected signal between 200 and 500 m is more intense, and it can be still interpreted as a lateral contribution from the dump and the area of tunnel entrance. Interestingly, a spot appears around 600 m in correspondence of the intersection among the track and the tunnel trajectory. This spot could be erroneously interpreted as the buried tunnels; however, an accurate analysis of its intensity has lead us to the conclusion that it more likely to be a lateral contribution associated to surface targets, consistent with presence of man-made structures in the area of the tunnel entrance. This hypothesis is corroborated by the fact that a spot having similar intensity arises around 800 m for the presence of a concrete house on the hilltop. The strongest reflection at the end of the profile at 1200 m is caused by the presence of a river.

Finally, we present data collected on the opposite side of the hill along the scan between points E and F, which intersects the tunnels at around 900 m (see Fig. 8). The tomographic reconstruction shows lateral returns due to the terrain topography and a fuel station, but also two subsurface spots (features X and Y in Fig. 8) located at about 880 m and 930 m (consistent with the expected tunnels' location) and at a free-space depth of about 40 m. By taking into account that the soil is a dry clay one with relative permittivity in the range 4-10 in VHF band [22], the effective depth of these targets is roughly 13-20 m. In conclusion, this outcome might be consistent with true depth of the tunnels which are buried at about 15 m.

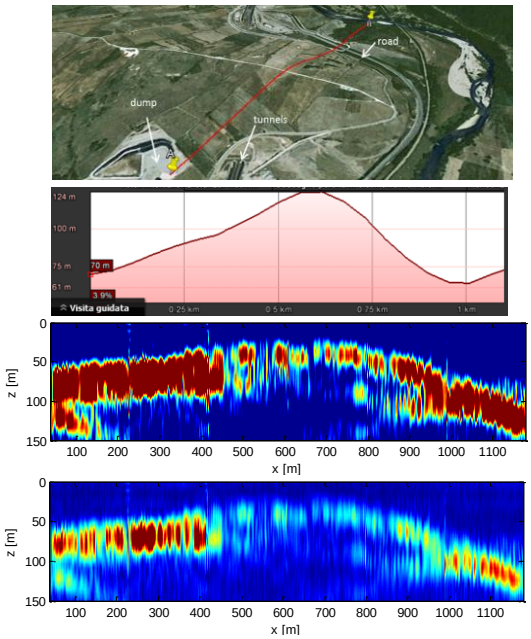

Figure 6 First panel: Aerial view of the surveyed zone on the highway in Southern Campania. The flight track is the red line between points A and B. Second panel: Elevation profile from Google Earth. Third panel: Tomographic reconstruction highlighting the surface topography. Fourth panel: Tomographic reconstruction showing details on the probed region.

V. Conclusions

A multi-mode and multi-frequency VHF/UHF airborne radar has been presented. The system is flexible to fit different needs depending on flight campaigns, thanks to the capability to switch between sounder and imager mode simply by setting few parameters during the flight. The experimental validation for the sounder modality has provided encouraging preliminary results and confirmed the system potentialities. At the same time, the experiments highlight the inherent difficulties of data interpretation in challenging environments, suggesting possible strategies to improve the system reliability. In fact, the frequency bandwidth of the sounder should be improved; in this frame an effort is ongoing to enlarge the operating bandwidth at 40 MHz. The other requirement, related to the above one, regards the necessity to better identify the lateral contributions. In this case, a possible solution is to perform repeated flight passages on the same

area so to acquire multiple parallel tracks, which can enable the use of 3D tomographic reconstruction approaches. Other future activities concern the possibility to assess foliage scattering and foliage penetration capabilities. The improvement of the UHF system at 900 MHz with 80 MHz bandwidth and a polarimetric antenna, as well as the relevant flight validation, is currently under development.

ACKNOWLEDGMENTS

The authors thank the anonymous reviewers for the perceptive and helpful suggestions, which have improved the manuscript.

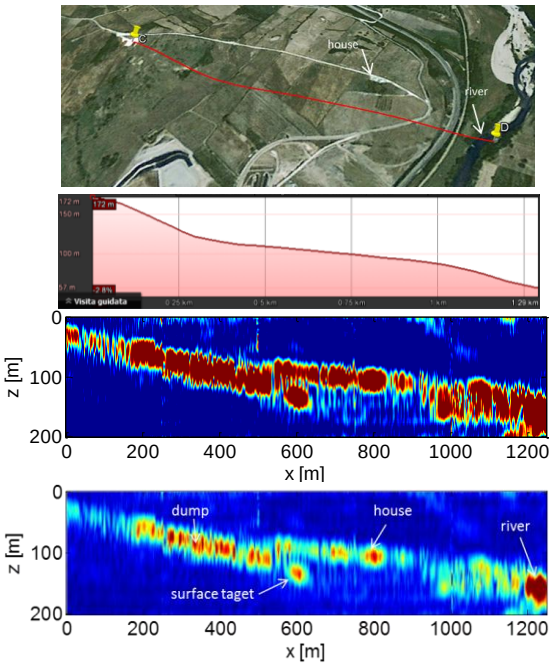

Figure 7 First panel: Aerial view of the flight track among points C and D. Second panel: Elevation profile of the terrain from Google Earth. Third panel: Tomographic reconstruction highlighting the surface topography. Fourth panel: Tomographic reconstruction showing details on the probed region.

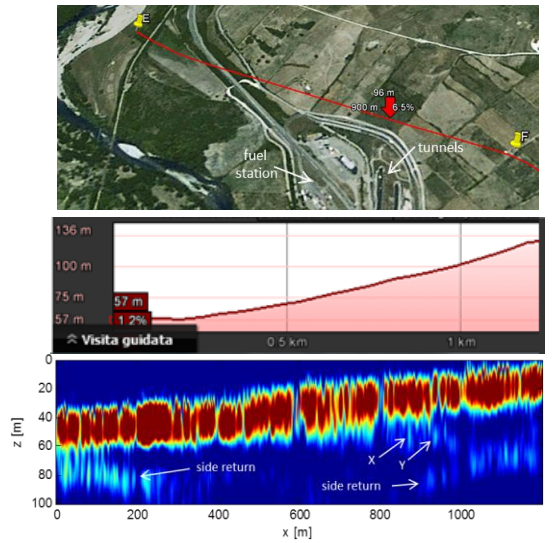

Figure 8 First panel: Aerial view of the flight track among points E and F. Second panel: Elevation profile of the terrain from Google Earth. Third panel: Tomographic reconstruction.

REFERENCES

[1] H. Hellsten, L. M. Ulander, A. Gustavsson, and B. Larsson, "Development of VHF CARABAS II SAR," *Proc. SPIE Radar Sensor Technology*, 2747, pp. 48-60, 1996.

[2] E. G. Njoku, W. J. Wilson, S. H. Yueh, S. J. Dinardo, F. K. Li; T. J. Jackson, V. Lakshmi, J. Bolten, "Observations of soil moisture using a passive and active low-frequency microwave airborne sensor during SGP99," *IEEE Trans. Geosci. Remote Sens.*, vol .40, no. 12, pp. 2659-2673, 2002.

[3] G. Smith-Jonforsen, L. M H Ulander, L. Xianyun "Low VHF-band backscatter from coniferous forests on sloping terrain," *IEEE Trans. Geosci. Remote Sens.*, vol.43, no.10, pp.2246-2260, 2005.

[4] L. M. H. Ulander, M. Lundberg, W. Pierson, and A. Gustavsson, "Change detection for low-frequency SAR ground surveillance," *IEE Proc. Radar, Sonar and Navigation*, vol. 152, no. 6, pp. 413-420, 2005.

[5] H. Machguth, O. Eisen, F. Paul, and M. Hoelzle, "Strong spatial variability of snow accumulation observed with helicopter-borne GPR on two adjacent Alpine glaciers," *Geophysical Research Letters*, vol. 33: pp. 1-5, 2006.

[6] I. A. Kalmykov, V. N. Tsymbal, V. B. Yefimov, "The using multifrequency airborne radar complex MARS for subsurface remote sensing," *Proc. of European Microwave Conference*, vol. 3, pp. 4, 2005.

[7] M. Davies, *Foliage penetration radar: detection and characterization of objects under trees*, SciTech, 2011.

[8] I. Catapano, L. Crocco, Y. Krellmann, G. Triltzsch, and F. Soldovieri, "A tomographic approach for helicopter-borne ground penetrating radar imaging," *IEEE Geosci. Remote Sens. Lett.*, vol. 9, no. 3, pp. 378-382, 2012.

[9] I. Catapano, L. Crocco, and F. Soldovieri, "Airborne ground penetrating radar imaging of buried targets: A tomographic approach", *Proc. of Advanced Ground Penetrating Radar (IWAGPR)*, 22-24 June 2011.

[10] H. Schimpf, A. Wahlen, H. Essen, "High range resolution by means of synthetic bandwidth generated by frequency-stepped chirps," *Electronics Letters*, vol. 39, no. 18, pp. 1346-8, 2003.

[11] A. Potsis, A .Reigber and K.P. Papathanas, "A phase preserving method for RF interference suppression in P-band synthetic aperture radar interferometric data," *Proc. of International Geoscience and Remote Sensing Symposium (IGARSS)*, 1999.

[12] J. Dall "A New Frequency Domain Autofocus Algorithm for SAR", *Proc. of the International Geoscience and Remote Sensing Symposium, IGARSS '91*, Helsinki, June, 1991.

[13] Z. Yunhua, W. Jie, L. Haibin, "Two Simple and Efficient Approaches for Compressing Stepped Chirp Signals", *Proc. of the 2005 Asia-Pacific Microwave Conference APMC2005*, vols. 1-5, pp 690-693, Suzhou, China, 4-7 Dec. 2005.

[14] I. G. Cumming, F. H.Wong, *Digital processing of Synthetic Aperture Radar data*, Artech House, 2005.

[15] J. C. Curlander, R.N. McDonough, *Synthetic aperture radar*, John Wiley & Sons, Inc.

[16] P. H. Eichel and C. V. Jakowatz Jr, "Phase-gradient algorithm as an optimal estimator of the phase derivative," *Optics Letters*, vol. 14, no. 20, pp. 1101-1103, 1989.

[17] C. V. Jakowatz Jr, and D. E. Wahl, "Eigenvector method for maximum-likelihood estimation of phase errors in synthetic-aperture-radar imagery," *Journal Optical Society America A*, vol. *10, no.* 12, pp. 2539-2546, 1993.

[18] D. E. Wahl, P. H. Eichel, D. C. Ghiglia, C. V. Jakowatz Jr., "Phase gradient autofocus-a robust tool for high resolution SAR phase correction," *IEEE Trans. Aerospace and Electronic Systems*, vol. 30, no. 3, pp. 827-835, 1994.

[19] A Moreira, J. Mittermayer, and R. Scheiber, "Extended chirp scaling algorithm for air and spaceborne SAR data processing in stripmap and ScanSAR imaging modes," *IEEE Trans. Geosci. Remote Sens.*, vol. 34, no. 5, 1996.

[20] A. Moreira and H. Yonghong "Airborne SAR processing of highly squinted data using a chirp scaling approach with integrated motion compensation," *IEEE Trans. Geosci. Remote Sens.*, vol. 32, no. 5, pp.1029-1040, 1994.

[21] M. Bertero and P. Boccacci, *Introduction to Inverse Problems in Imaging*, Inst. of Physics, Bristol Philadelphia, UK, 1998.

[22] D. J. Daniels, *Ground penetrating radar*, Institution of Electrical Engineers, 2004.